Scientific Reports

https://doi.org/10.1038/s41598-026-46139-z

Article in Press

Effect analysis of soil texture and water content on soil adhesive force based on the discrete element method

Received: 1 December 2025

Accepted: 24 March 2026

Published online: 05 May 2026

Cite this article as: Jeong D., Kim M., Choi S. *et al.* Effect analysis of soil texture and water content on soil adhesive force based on the discrete element method. *Sci Rep* (2026). https://doi.org/10.1038/s41598-026-46139-z

Dae-Wi Jeong, Min-Seung Kim, Se-O Choi, Shin-Young Noh, Yeon-Soo Kim, Wan-Soo Kim, Seung-Yun Baek & Yong-Joo Kim

Effect analysis of soil texture and water content on soil adhesive force based on the discrete element method

Dae-Wi Jeong [a], Min-Seung Kim [a], Se-O Choi [a], Shin-Young Noh [a], Yeon-Soo Kim [a,b,*], Wan-Soo Kim [c,d], Seung-Yun Baek [e] and Yong-Joo Kim [f, g, *]

[a] *Department of Bio-Industrial Machinery Engineering, Pusan National University, Miryang 50463, Republic of Korea*

[b] *Major of Natural Resources Systems Engineering, Pusan National University, Yangsan 50612, Republic of Korea*

[c] *Department of Smart Bio-Industrial Mechanical Engineering, Kyungpook National University, Daegu 41566, Republic of Korea*

[d] *Upland Field Machinery Research Center, Kyungpook National University, Daegu 41566, Republic of Korea*

[e] *Eco-friendly Hydrogen Electric Tractor & Agricultural Machinery Institute, Chungnam National University, Daejeon 34134, South Korea*

[f] *Department of Smart Agricultural System Mechanical Engineering, Chungnam National University, Daejeon 34134, Republic of Korea*

[g] *Department of Smart Agriculture Systems, Chungnam National University, Daejeon 34134, Republic of Korea*

Abstract

Understanding soil–metal adhesion under varying moisture and texture conditions is essential for predicting soil–tool interactions in agricultural machinery. However, despite its importance, research that directly quantifies soil adhesion and provides physically based parameters for

modeling remains limited, particularly across the diverse conditions encountered in field operations. In this study, we experimentally measured soil–metal adhesion across multiple penetration speeds and integrated the results with discrete element method (DEM) simulations based on the Edinburgh Elasto-Plastic Adhesion (EEPA) model. Adhesion tests were conducted for three soil textures (sandy loam, sandy clay loam, and loam) and four water contents (10–25%) at penetration speeds of 50 and 500 mm·min^{-1}. Adhesive force increased with water content and peaked near the liquid limit (20–25%), while remaining nearly independent of penetration rate (<5% variation). DEM calibration showed that surface energy ($\Delta\gamma$) is the dominant parameter governing compressive behavior, whereas the constant pull-off force (f_0) primarily controls adhesive strength. Two-way ANOVA confirmed that these mechanisms operate independently ($p > 0.05$). The calibrated model achieved $R^2 \geq 0.93$ and RMSE ≤ 0.1 N across all textures, and validation at an intermediate speed of 250 mm·min^{-1} demonstrated stable predictive performance ($R^2 \geq 0.93$ for compression; $R^2 \geq 0.98$ for adhesion). By linking multi-speed adhesion measurements with a physically based DEM contact model, this work establishes a robust and transferable $\Delta\gamma$–f_0 calibration framework for modeling soil adhesion in cohesive soils.

Keywords: soil adhesion, soil texture, water content, soil-tool interaction, discrete element method

1. Introduction

Predicting soil-induced loads is a fundamental requirement in the design and operation of agricultural and off-road machinery. Under field conditions, soil–tool and soil–tire interactions govern draft force, power take-off (PTO) load, traction performance, fuel consumption, and clogging behavior, all of which determine the economic efficiency and productivity of mechanized[1-3]. Numerous experimental studies have shown that variations in soil physical properties and operating conditions can substantially alter machine power demand and mobility[4-6], emphasizing the need for predictive tools capable of capturing soil–machine mechanical behavior across diverse field environments. Reliable load prediction systems therefore play a crucial role in reducing trial-and-error during implement development, optimizing powertrain specifications, and improving overall work efficiency.

To establish such predictive capabilities, simulation-based approaches have been widely adopted for analyzing soil–machine interaction. Multi-body dynamics (MBD), finite element method (FEM), and discrete element method (DEM) simulations have been employed to investigate implement frame stresses, soil disturbance patterns, and tractor power requirements under various tillage and harvesting conditions[7-10]. Among these numerical techniques, DEM has become a

central Terramechanics tool because it represents particle-scale contact mechanics, soil failure, and large deformation under tool loading with high physical interpretability[11,12], enabling effective prediction of soil mechanical responses across a wide range of agricultural operations. Building on these capabilities, numerous studies have demonstrated the applicability of DEM for modeling soil behavior under realistic field conditions. Previous studies have demonstrated the applicability of DEM for predicting draft force, rotary tillage loads, and PTO power requirements under cohesive soil conditions[13-17]. These studies consistently showed that tillage depth, travel speed, particle-size distribution, and soil surface energy strongly govern soil deformation patterns and machine load responses.

In parallel, an additional body of research has focused on adhesion mechanisms at soil–tool interfaces, providing insights highly relevant to the present study. Previous studies have quantified the effects of soil moisture, texture, surface material, and interface geometry on soil–tool adhesion and detachment behavior[18-21]. Collectively, these DEM-based and adhesion-focused studies have advanced understanding of soil mechanical behavior and soil–tool interface phenomena, providing a foundation for more accurate modeling of tool resistance and adhesion-related mechanisms in cohesive soils.

Despite these advances, most DEM calibration efforts continue to rely primarily on reproducing bulk mechanical responses such as compressive resistance or shear behavior, while soil–metal adhesion is

typically treated as a secondary or indirectly adjusted parameter. In many DEM applications, adhesion is approximated using simplified cohesion constants or surface-energy-based contact laws that are tuned to match macroscopic force measurements rather than being independently calibrated or experimentally validated at the soil–tool interface. More importantly, existing studies typically vary one factor at a time—such as soil texture, water content, or operating speed—while keeping the remaining conditions fixed. As a result, the combined and interacting effects of soil texture, moisture state, and loading rate on soil–metal adhesion have not been systematically quantified or incorporated into DEM calibration frameworks. This limitation restricts the transferability of calibrated adhesion parameters across realistic field conditions, where these factors inevitably vary simultaneously.

Previous DEM studies on cohesive granular materials have explicitly pointed out that such simplified adhesion formulations do not adequately account for contact history, plastic deformation, or the evolution of real contact area, which are critical for physically realistic modeling of wet and cohesive materials[22]. As a result, adhesion-related parameters are often over-adjusted to compensate for missing physical mechanisms, leading to limited transferability and reduced predictive reliability when DEM models are applied across different soil textures and moisture conditions.

Accordingly, the objectives of this study are to:

(1) experimentally quantify soil–metal adhesive forces under controlled combinations of soil texture and water content using a cone penetration–extraction test;

(2) examine the sensitivity of soil adhesion to penetration speed in order to distinguish quasi-static and rate-dependent behaviors;

(3) calibrate key adhesion-related parameters of the Edinburgh Elasto-Plastic Adhesion (EEPA) model based on the measured adhesion forces; and

(4) validate the transferability of the calibrated parameters across different soil textures, moisture conditions, and loading rates.

To address these limitations, the present study developed a dedicated measurement system capable of directly quantifying soil–metal adhesive forces using controlled cone penetration–extraction tests. The experimental procedure was designed with reference to standardized soil physical testing methods[23,24] and recent adhesion-focused measurement practices[25]. Adhesion was measured for three soil textures (sandy loam, sandy clay loam, loam), four water contents spanning the plastic to liquid range, and multiple penetration speeds to capture rate-dependent behavior. This multi-condition dataset provides a systematic basis for characterizing moisture-, texture-, and velocity-dependent adhesion in cohesive soils.

To numerically reproduce the experimentally observed adhesion behavior, the Edinburgh Elasto-Plastic Adhesion (EEPA) model

implemented in DEM simulations was adopted in this study[26,27]. Surface energy ($\Delta\gamma$) and pull-off force (f_0) governing particle-to-geometry adhesion were calibrated using experimental data across different soil textures and water content conditions.

2. Materials and Methods

2.1. Soil Properties Measurement

In this study, the compressive force refers to the maximum normal reaction force measured during the penetration phase, reflecting soil resistance to tool intrusion. The adhesive force is defined as the peak tensile force recorded during the extraction phase, representing soil–tool adhesion after unloading.

To analyze the effects of soil texture on adhesion, three representative fields (sandy loam, sandy clay loam, and loam) were selected (Fig. 1). Soil samples were collected from the 0–10 cm surface layer, as this zone directly interacts with tillage implements. According to the principle that soil texture is determined by the relative proportions of sand, silt, and clay, characterizing these fractions was essential for identifying physical soil properties. To further evaluate the influence of soil moisture on soil–tool interactions, Atterberg limit tests were performed to determine the plastic and liquid limits, from which the plasticity index was calculated. Soil texture was classified according to the USDA soil texture method[23], and the results together with the Atterberg limits (plastic limit, liquid limit, and plasticity index) are

summarized in Table 1. These measurements provided the basis for analyzing the transition of soils from solid to plastic and liquid states under varying water contents, and for interpreting the subsequent adhesion tests and DEM simulations. Permission to collect soil samples from the experimental fields was obtained from the field managers and landowners. No protected or restricted areas were used, and no endangered species were involved in the sampling procedure.

As shown in Fig. 2, soil samples required for adhesion measurement were prepared following a standardized procedure. Soil collected from the three fields was first oven-dried at 110 °C for 24 hours. The dried soil was then crushed and sieved through a 2 mm mesh, followed by a secondary sieving through a 0.425 mm mesh in accordance with the KS F 2303 standard[28] for Atterberg limit testing. To adjust soil moisture, water equivalent to six target contents (5–30% on a dry basis) was added to the sieved soil. Although soil samples were initially prepared over a nominal moisture range of 5–30% (dry basis), preliminary tests showed that adhesive force measurements at the extremes were unreliable. At low moisture content (5%), insufficient cohesion resulted in unstable pull-off behavior, whereas at high moisture content (30%), near-saturated conditions led to excessive soil deformation and loss of repeatability, particularly for sandy loam. Accordingly, four representative moisture levels (10, 15, 20, and 25%) were selected for

detailed analysis, spanning the plastic to near-liquid consistency range as identified by Atterberg limits. These discrete intervals were chosen to capture the progressive development of soil–metal adhesion while maintaining experimental stability and reproducibility. The soil was thoroughly mixed using a scraper to ensure uniform water distribution and then packed into acrylic containers with a height of 40 mm. Compaction was applied using a tamper, after which the containers were covered with a wet cloth and stored for 1 h to allow equilibration before testing.

2.2. Soil adhesive force measurement system

The soil–tool adhesion was measured using a custom-built test system[29]. Fig 3 shows the experimental setup used to measure soil–metal adhesive forces, including the stainless-steel cone, load cell, and vertical actuation system. In addition to the experimental hardware, Fig. 3 includes a schematic illustration of the cone–soil contact during penetration and extraction, highlighting the adhesion interface that governs the measured pull-off force. The setup consisted of a stainless steel cone connected to a load cell (SBA-100L, CAS, Korea) with a capacity of 150 kgf and a resolution of 20 g. The load cell was interfaced with an indicator (CI-600A, CAS, Korea) and a data acquisition program (GP WORKS, CAS, Korea), as summarized in Table 2. The test cone was fabricated from SS401 structural steel using a conventional turning

process without polishing or coating, and had a top angle of 54.4°, a generatrix length of 35 mm, a base diameter of 32 mm, and a cylinder height of 30 mm, corresponding to a nominal contact area of 1.649×10^{-3} m² (Table 3). The same cone was used consistently throughout all experiments and DEM simulations, ensuring identical material, geometry, and surface conditions. The surface roughness of the stainless-steel cone was measured using a surface profilometer to quantitatively characterize the tool surface condition. Measurements were taken at three locations on the same cone surface. The arithmetic average roughness (Ra) ranged from 0.70 to 0.96 μm with a mean value of 0.85 ± 0.13 μm, while the corresponding Rz values ranged from 2.32 to 3.32 μm. The cone was fabricated by conventional turning without polishing or coating, and the same cone was used consistently throughout all experiments and DEM simulations to maintain identical surface conditions.

2.3. Experimental Method for Soil Adhesive Force

The stainless-steel cone was vertically penetrated into the soil sample to a depth of 30 mm and then extracted to measure adhesion forces. Two penetration speeds (50 and 500 mm·min^{-1}) were employed to evaluate the rate dependence of compressive soil resistance. The selected penetration speeds were not intended to directly replicate the absolute operating speeds of full-scale agricultural machinery. Instead, the experimental setup was designed to represent distinct loading-rate regimes relevant to soil–tool interaction mechanisms. In this context, the lower speed (50 mm·min^{-1}) represents quasi-static penetration

conditions, whereas the higher speed (500 mm·min^{-1}) corresponds to a moderate-rate regime in which rate-dependent soil resistance becomes apparent. Given the scaled geometry of the test apparatus, direct kinematic similarity with field-scale operations is not required. Rather, the objective was to capture relative changes in compressive and adhesive responses across penetration rates, enabling physically meaningful calibration and validation of DEM parameters governing rate-sensitive behavior.

In contrast, the extraction speed was fixed at 5 mm·min^{-1} for all tests to ensure quasi-static conditions during adhesion measurement. Variations in penetration speed may influence drainage conditions in cohesive soils, particularly at higher water contents. In the present experimental setup, soil samples were prepared in shallow containers (40 mm height) with a free upper surface, allowing partial dissipation of pore water during penetration and extraction. Given the relatively low penetration speeds investigated (50–500 mm·min^{-1}), the tests are interpreted as representing partially drained to quasi-drained conditions rather than fully undrained behavior. A schematic illustration of the cone penetration–extraction test procedure is provided in Fig. 4.

The higher penetration speed (500 mm·min^{-1}) was selected to enhance experimental efficiency and to approximate the order of magnitude of local soil–tool interaction velocities rather than the forward travel speed of agricultural machinery. Previous experimental studies on rotary tillage have shown that soil resistance and tool loading are

governed by the local interaction conditions experienced by individual tool elements, which occur at substantially lower effective penetration rates than the machine travel speed[32]. The adhesive force was defined as the maximum tensile load recorded during cone extraction. Each condition (three soil textures × four water contents) was repeated ten times, resulting in a total of 120 measurements.

2.4. DEM Modeling Environment Using the EEPA Model

To reproduce soil–tool interactions in a virtual environment, a DEM framework was constructed using the Edinburgh Elasto-Plastic Adhesion (EEPA) model implemented in EDEM software. The EEPA model was developed to capture the history-dependent behavior of cohesive granular solids, where flow and handling properties are strongly influenced by prior consolidation stress. It combines a nonlinear hysteretic spring formulation to describe elastic–plastic deformation with an adhesion component that depends on the plastic contact area[25,27].

The total normal contact force is expressed as the sum of the hysteretic spring force and the viscous damping term:

$$F_n = F_{n,\,hys} + F_{n,\,damp} \quad (1)$$

where $F_{n,\,hys}$ is the hysteretic spring force and $F_{n,\,damp}$ is the damping force proportional to the relative normal velocity. The hysteretic spring force incorporates both elastic–plastic loading and adhesion:

$$F_{n,\,hys} = k_1\delta^n + f_0 + K_{adh}(\delta - \delta_p)^X \quad (2)$$

where k_1 is the loading stiffness, δ is the overlap, n is the stiffness exponent, f_0 is the constant pull-off force, K_{adh} is the adhesive stiffness parameter, δ_p is the plastic overlap, and X is the adhesion power value. The resulting force–displacement behavior under loading and unloading is illustrated in Fig. 5.

The damping term is defined as:

$$F_{n,\,damp} = -c_n\dot{\delta} \quad (3)$$

with $c_n = -2\sqrt{m^* k_1}\ln e/\sqrt{\pi^2 + (\ln e)^2}$ where m^* is the equivalent particle mass and

e is the restitution coefficient.

The tangential force is modeled as a spring–dashpot system constrained by a modified Coulomb limit:

$$F_t = \min(k_t\Delta s + c_t v_t, \mu(F_n + F_{adh}) \quad (4)$$

where k_t is the tangential stiffness, c_t is the tangential damping coefficient, Δs is the incremental tangential displacement, v_t is the tangential velocity, and μ is the static friction coefficient.

Rolling resistance is additionally included as:

$$T_r = -\mu_r F_n R \frac{\omega}{|\omega|} \quad (5)$$

where μ_r is the rolling resistance coefficient, R is the contact radius, and ω is the angular velocity at contact.

In addition to conventional contact parameters, the EEPA model includes a set of adhesion–plasticity parameters, as described in previous studies[25,13] . The complete list of parameters and their roles are summarized in Table 4. While Table 4 summarizes the full set of parameters involved in the EEPA contact formulation, not all parameters were treated as calibration variables in this study.

Based on their roles, the parameters were classified into fixed shape-related parameters and calibrated adhesion-related parameters. The overall DEM modeling, calibration, and validation workflow adopted in this study, including parameter classification and the iterative calibration loop, is summarized in Fig. 6. The EEPA parameters implemented in the DEM simulations, together with their numerical values and contact pairs, are summarized in Table 5. As shown in Table 5, surface energy ($\Delta\gamma$) and constant pull-off force (f_0) were treated as calibration parameters, while

the remaining shape-related parameters were fixed based on validated literature values. The fixed EEPA parameters were adopted from a validated DEM–MBD study on rotary tillage conducted under cohesive soil conditions[34], in which the same parameter set achieved prediction accuracies exceeding 90% for PTO power and draft force. By adopting this previously validated parameter set, the present study ensures numerical robustness and software-independent reproducibility of the EEPA contact model.

In addition to the EEPA-specific adhesion and plasticity parameters, frictional interactions were explicitly included in the DEM model. The static friction, rolling friction, and restitution coefficients applied to soil–soil and soil–steel contacts are summarized in Table 6 for sandy loam soil. This parameter set represents the baseline DEM soil model, against which sandy clay loam and loam soils were treated as cohesive soils with modified frictional properties. For sandy clay loam and loam soils, which have higher clay contents and exhibit cohesive behavior, a separate set of frictional and restitution parameters was adopted, as summarized in Table 7. These soils were treated as cohesive soils, reflecting reduced friction coefficients and enhanced rolling behavior reported in previous DEM studies on cohesive materials. These parameters were kept constant across all simulations to isolate normal and adhesive contact behavior. Under the present vertical penetration–extraction configuration, the measured axial force was dominated by normal contact and adhesive interactions, while the contribution of tangential frictional forces was secondary. The influence of friction-related parameters under

sliding-dominated or oblique soil–tool interactions is acknowledged as a limitation and will be investigated in future studies. The detailed calibration and validation procedures for the EEPA parameters are described in Section 2.7.

2.5. DEM Soil Modeling Method

Three soil textures—sandy loam, sandy clay loam, and loam—were considered for DEM modeling. The DEM soil parameters for sandy loam were adopted from the baseline parameter set summarized in Table 6, whereas sandy clay loam and loam were modeled using the cohesive soil parameter set shown in Table 7. Although the experimental program originally included six target water contents (5, 10, 15, 20, 25, and 30% on a wet basis), adhesion forces could not be reliably measured at the extremes of 5% and 30%. Therefore, only four representative moisture levels (10, 15, 20, and 25%) were used in the DEM calibration and validation, resulting in a total of 12 soil beds (three textures × four moisture levels).

For each condition, soil specimens were collected in cylindrical molds (diameter 8.8 cm) and weighed to determine the wet mass. After subtracting the container mass, the dry mass was calculated using the wet-basis water content, and the dry bulk density was obtained as the ratio of dry mass to specimen volume. All values of dry soil mass, water

mass, and specimen height reported in Table 8 represent the averages of ten repeated adhesion experiments. The wet and dry bulk densities were then calculated from these averages, and their corresponding standard deviations across the ten replicates are also presented in the table. The measured bulk densities ranged approximately from 1.05 to 1.40 g cm^{-3}, with values tending to increase with higher water content due to packing and compaction effects during specimen preparation[35].

Given wet-basis water content ω_{wb} and wet mass m_{wet}, the dry mass was calculated as $m_{dry} = m_{wet}(1 - \omega_{wb})$. The cylindrical specimen volume V was determined from the measured height, and the dry bulk density was then defined as $\rho_b = \frac{m_{dry}}{V}$.

In DEM, the experimentally measured bulk density was reproduced by adjusting the particle density (rather than particle mass) while keeping the particle size distribution constant. The solid density of particles was tuned until the simulated solid fraction matched the target bulk density within ±2%. This ensured that the DEM soil beds reproduced the compaction and stiffness observed in experiments. The resulting particle masses corresponding to each soil–water content are summarized in Table 9, together with the measured and simulated bulk densities and their calibration errors.

For particle–particle interactions, the Edinburgh Elasto-Plastic Adhesion (EEPA) model was applied. The shape-related EEPA parameters—contact plasticity ratio, slope exponent, tensile exponent, and tangential stiffness multiplier—were kept constant across textures, following recommended ranges[35]. The dependence on water content was mainly reflected through surface energy, which was calibrated against adhesion tests in Section 2.7. The constant pull-off force was treated as an independent calibration parameter because it directly governed the adhesive (pull-off) response. While surface energy ($\Delta\gamma$) influenced the compressive behavior, f_0 was iteratively adjusted to match the measured adhesion magnitudes across moisture levels.

For each of the 12 texture–moisture combinations, ten DEM beds were generated with different random seeds to account for variability. These beds were used consistently in the subsequent cone penetration simulations.

Note: Although dry bulk density is theoretically independent of soil water content, the experimental results showed a slight increase at higher moisture levels. This trend is attributed to compaction and particle rearrangement facilitated by water during sample preparation, rather than an intrinsic change in soil density.

Although physical soil particles range from micrometer to millimeter scales, DEM simulations commonly adopt coarse-grained spherical particles to maintain computational feasibility during large-deformation soil–tool interaction analyses. In this study, a particle diameter of 10 mm was selected following the typical coarse-graining range (4–14 mm) reported in agricultural soil DEM studies[14,13]. This size enables stable contact detection, realistic force–displacement behavior, and practical computation time while preserving macroscopic soil responses such as penetration resistance and adhesion. The effects of moisture and soil texture were therefore represented through calibrated EEPA contact parameters rather than microscale particle geometry. As demonstrated in the validation results presented later, this coarse-grained representation was sufficient to reproduce the experimental compressive and adhesive forces with high accuracy. It should be noted that the use of mono-sized spherical particles may influence local packing structures and contact statistics at the microscopic scale. While this limitation does not affect the macroscopic force responses targeted in this study, future work will explicitly investigate the influence of particle size distribution on soil–tool interaction behavior.

Because coarse-grained DEM particles may introduce discretization-dependent contact statistics, potential size effects were considered in

relation to the cone geometry. In the present configuration, the cone base diameter (32 mm) corresponds to approximately 3.2 particle diameters (d = 10 mm), and the penetration–extraction response is governed by an ensemble of particle–cone contacts rather than by a single contact. Moreover, the DEM model was calibrated directly against experimentally measured macroscopic force–displacement responses (adhesive pull-off force and penetration resistance) and independently validated at a penetration speed not used for calibration. This calibration–validation strategy implicitly mitigates discretization-induced biases and supports the use of coarse-graining for the macroscopic force predictions targeted in this study. Nevertheless, we acknowledge that local packing structures and micromechanical contact statistics may differ from real soils; therefore, future work will evaluate particle size distributions and non-spherical shapes to quantify their influence on contact-level behavior.

2.6. Numerical Cone Penetration–Extraction Test

Numerical cone penetration–extraction tests were carried out for each of the 12 soil beds defined in Section 2.5. The stainless-steel cone geometry was modeled identical to that used in the experimental tool, including the half-angle and tip radius. The soil domain was constructed as a cylindrical container with a diameter of 88 mm and a height of 40

mm, and consisted of approximately 250–300 spherical particles with a diameter of 10 mm, depending on soil texture and bulk density. During penetration, the cone interacted with multiple particles simultaneously, ensuring force averaging over an ensemble of contacts rather than being dominated by an individual particle contact. Lateral walls were placed at least six cone diameters from the penetration axis and the container depth was more than four times the penetration depth to minimize boundary effects. The container base was set rigid and no-slip.

All DEM simulations were conducted using a fixed time step corresponding to 20% of the Rayleigh critical time step, which is a commonly adopted criterion to ensure numerical stability in explicit DEM calculations. This choice has been widely reported in previous DEM studies to provide a stable balance between computational efficiency and accurate resolution of contact dynamics. To verify numerical stability, additional simulations were conducted at an intermediate penetration speed (250 mm·min^{-1}), and no significant differences in force response trends were observed compared to the reference condition, confirming time-step independence within the investigated range. Soil particles were initially generated with a random spatial distribution above the specimen container without interparticle overlap. All particles were assigned zero initial velocity prior to the settling process. After

generation, gravitational settling was applied under Earth gravity while the container boundaries remained fixed and no external loading was imposed. Each DEM bed was allowed to settle under gravity for 0.1–0.2 s prior to loading. The settling process was considered complete when the average particle kinetic energy decreased to less than 1% of its peak value, indicating that the soil particle assembly had reached a quasi-static equilibrium state. The soil assembly was then subjected to penetration–extraction loading. The cone was driven vertically into the soil to a penetration depth of 30 mm and subsequently extracted along the same path. Two penetration/extraction speeds, 50 and 500 mm·min^{-1}, were simulated to evaluate rate sensitivity, with 500 mm·min^{-1} used as the reference condition for calibration and validation. All penetration–extraction tests were performed using the same steel cone with unchanged surface conditions to eliminate variability associated with tool surface properties.

The soil assembly was considered to reach a quasi-static equilibrium when the average particle kinetic energy decayed to less than 1% of its peak value and remained stable for a prescribed duration. The same settling protocol and equilibrium criterion were consistently applied to all simulations to minimize the influence of initial particle arrangement on the final soil bed structure.

The axial reaction force acting on the cone was recorded at every simulation timestep. The compressive force was defined as the maximum axial load during penetration, while the adhesive force was defined as the maximum tensile load (most negative axial force) during extraction. Fig. 7 illustrates the penetration–extraction process and the definition of compressive and adhesive forces based on the axial reaction force acting on the cone, together with a representative force–displacement response.

Compressive force was not used for calibration, since soil bulk density had already been matched to experimental values through particle mass adjustment (Section 2.5). Instead, calibration focused exclusively on adhesive force. In the EEPA model, surface energy ($\Delta\gamma$) was selected as the primary calibration parameter because it directly governs the magnitude of soil–metal adhesion and its dependence on soil water content. Although surface energy also influenced the compressive response, adjustments to the constant pull-off force (f_0) were found to more directly affect adhesive force.

Therefore, $\Delta\gamma$ and f_0 were treated as quasi-independent calibration parameters, with variations in $\Delta\gamma$ primarily influencing the compressive force response and variations in f_0 predominantly governing the adhesive (pull-off) force. This parameter–response relationship reflects the experimentally observed penetration–extraction force trends under

different soil moisture conditions. For validation, compressive force was retained as an independent metric that was not used during calibration. In addition, simulations at an intermediate penetration speed (250 mm·min^{-1}), which was not used for parameter fitting, were designed to evaluate model transferability across penetration rates.

The compressive force was retained as an independent validation metric. After calibrating adhesion, predicted penetration forces were compared with experimental measurements across all texture–moisture conditions. Good agreement within experimental variability was regarded as evidence that the DEM model reproduced not only adhesion but also the mechanical resistance of soil beds without further parameter tuning. Additionally, intermediate-speed (250 mm·min^{-1}) simulations were conducted for validation, using identical boundary and loading conditions to verify model transferability across penetration rates.

2.7. Calibration and Validation of the DEM Soil–Tool Interaction Model

In this study, DEM calibration was conducted through a structured, multi-step procedure designed to explicitly capture moisture-dependent soil–metal adhesion behavior. Model parameters were first classified into fixed parameters, determined from material properties and literature, and calibrated parameters, adjusted using experimental measurements. Among the EEPA contact parameters, the surface energy increment ($\Delta\gamma$) and pull-off force parameter (f_0) were selected for calibration based on

their direct influence on compressive resistance and adhesive force, respectively.

Calibration was performed using experimental data obtained at a penetration speed of 500 mm·min^{-1}, with $\Delta\gamma$ adjusted to reproduce moisture-dependent trends and f_0 tuned to match the absolute magnitude of the measured pull-off force. Calibration quality was evaluated using multiple statistical criteria, including the coefficient of determination (R^2), root mean square error (RMSE), and mean absolute percentage error (MAPE). To verify model generality, validation was conducted under conditions not used for calibration, including an intermediate penetration speed of 250 mm·min^{-1}. Agreement between experimental and simulated results across soil textures and moisture levels was used to assess the robustness and transferability of the calibrated parameters.

Calibration was performed at a penetration speed of 500 mm·min^{-1} by adjusting surface energy ($\Delta\gamma$) and pull-off force (f_0) to reproduce the experimentally measured adhesion trends with soil water content. Measured bulk density was directly applied during soil bed initialization and was not used as a calibration variable. Fig. 8. summarizes the overall calibration and validation workflow, including the use of experimental bulk density, adhesive force, and compressive force data.

Independent validation was conducted using compressive penetration force, which was not employed during calibration, across all soil texture–moisture combinations. In addition, cross-validation at a lower penetration speed (50 mm·min^{-1}) and an intermediate speed (250

mm·min^{-1}) confirmed that predicted adhesive forces remained within experimental variability, indicating weak rate sensitivity within the tested range. This calibration approach is consistent with previous DEM studies on cohesive soils, in which surface-energy-based parameters were tuned to reproduce experimentally measured soil–tool adhesion behavior[13].

Model performance was considered satisfactory when adhesion trends with water content were reproduced, compressive resistance increased monotonically with moisture content, and statistical criteria were satisfied ($R^2 > 0.9$; RMSE ≤ experimental standard deviation). The validated DEM model was subsequently used for prediction and extended simulations under varying soil and tool conditions.

3. Results

3.1. Compressive and Adhesive Force Characteristics under Different Penetration Speeds

The compressive and adhesive forces measured at two different penetration speeds (500 and 50 mm·min^{-1}) are summarized in Tables 10 and 11. At 500 mm·min^{-1}, peak compressive forces occurred at 15% water content for all three soils, whereas values at 50 mm·min^{-1} were reduced by approximately 35% on average. This rate dependency suggests that higher penetration velocity is associated with increased

soil resistance, as also reflected in the DEM simulations. DEM simulations reproduced the same trend, indicating that viscous damping and elasto-plastic contact effects contributed to the observed increase in compressive force.

Fig. 9 presents representative force–displacement curves obtained from cone penetration–extraction tests conducted at two different penetration speeds. As shown in Fig. 9A, the force–displacement curves measured at a penetration speed of 500 mm·min^{-1} exhibit substantially higher compressive forces during the penetration phase for all soil textures, indicating a pronounced rate-dependent strengthening effect. In contrast, Fig. 9B shows the corresponding force–displacement behavior at a lower penetration speed of 50 mm·min^{-1}, representing quasi-static loading conditions. Under this condition, compressive forces are consistently reduced compared to those in Fig. 9A, while the overall shape of the force–displacement response remains similar. Notably, despite the clear difference in compressive behavior between Fig. 9A and Fig. 9B, the peak adhesive (pull-off) forces observed during extraction are comparable across the two penetration speeds, indicating that soil–metal adhesion is quasi-rate-independent within the tested range.

In contrast, the adhesive forces—the peak tensile forces measured during extraction—showed only marginal sensitivity to penetration rate.

At 500 mm·min^{-1}, the maximum adhesive forces were 1.76 N (sandy loam, 20%), 1.96 N (sandy clay loam, 25%), and 2.16 N (loam, 25%), while at 50 mm·min^{-1}, similar values of 1.79 N, 2.04 N, and 2.22 N were recorded. The difference between the two speeds was less than 5%, suggesting that adhesion is quasi-rate-independent within the tested range.

3.2. Surface-Energy and Pull-Off Force Calibration for Adhesive Force

3.2.1. *Rationale and setup*

Following Sections 2.4–2.7, the EEPA contact model was used to reproduce soil–tool adhesion. Bulk density of each soil bed (10–25% water content; three textures) was fixed to the measured values (Table 9). Adhesion was calibrated at a penetration speed of 500 mm·min^{-1} with extraction fixed at 5 mm·min^{-1}. Among the EEPA parameters, $\Delta\gamma$ and f_0 were selected for calibration. $\Delta\gamma$ was adjusted to reproduce moisture-dependent force trends, while f_0 was used to match the absolute magnitude of adhesive force. Friction and restitution parameters were held within the ranges validated in Section 2.5.

3.2.2. *Calibration procedure and objective*

For each texture $s \in \{\text{sandy loam, sandy clay loam, loam}\}$ and water content $w \in \{10,15,20,25\}$,

DEM penetration–extraction tests (30 mm depth) were repeated with different random seeds (n = 10) and the peak tensile load during

extraction was converted to adhesion pressure using the nominal cone area.

Calibration minimized the discrepancy between experimental and simulated adhesion by jointly adjusting the $\Delta\gamma$ and f_0:

Both parameters were tuned within physically reasonable ranges ($\Delta\gamma$ = 0.1-1.0 J m^{-2}; f_0 = -0.01-0.15 N) to maintain monotonic trends with water content and stability of the soil bed.

$$\min_{\{\Delta\gamma(s,\omega)\}} \sum_s \sum_\omega \left[\frac{\bar{A}_{sim}(s,\omega;\, \Delta\gamma,\, f_0) - A_{exp}(s,\omega)}{A_{exp}(s,\omega)} \right]^2 \quad (6)$$

subject to monotonicity in moisture for each texture (i.e., $\Delta\gamma$ (s,10) ≤ $\Delta\gamma$ (s,15) ≤ $\Delta\gamma$ (s,20) ≤ $\Delta\gamma$ (s,25)) and physically consistent scaling of f_0 with adhesion magnitude.

Pointwise calibrated values $\Delta\gamma$ (s,w) at the four moisture levels (Table 8).

A smooth mapping $\Delta\gamma$s (w) per texture (piecewise-linear or quadratic fit) for interpolation/extrapolation in Section 3.3.

3.2.3. *Calibration outcome*

Calibration results indicated that adjusting $\Delta\gamma$ primarily influenced the compressive force response, whereas variation of f_0 scaled the magnitude of adhesive force. Excellent agreement was achieved across all textures and moisture levels (R^2 ≥ 0.90, RMSE ≤ experimental SD per condition). Calibrated $\Delta\gamma$ increased monotonically with water content from 10 to 25%, consistent with the growth of capillary bridge area and

effective contact area. In contrast, variations in f_0 were primarily responsible for reproducing the absolute magnitude of adhesion at each moisture level.

Distinct trends were observed between compressive force responses associated with $\Delta\gamma$ and adhesive force magnitudes associated with f_0 across the tested conditions. The relative error of peak adhesion was $\leq$ 5% for sandy loam and loam, and $\leq$ 7% for sandy clay loam at 25% water.

Cross-checks at 50 mm·min^{-1} (not used for calibration) showed that predicted adhesion remained within experimental scatter ($\leq$ 5%), indicating weak rate sensitivity and supporting the use of 500 mm·min^{-1} as the reference calibration speed. The calibration results are summarized in Tables 12 and 13, which present the fitted surface-energy and pull-off-force parameters for each soil texture and water content.

3.3. Validation of Adhesive and Compressive Behavior at Intermediate Penetration Speed

3.3.1. *Objective and validation setup*

This section aims to evaluate the predictive reliability of the calibrated DEM model under intermediate penetration speeds that were not included in the calibration phase. $\Delta\gamma$ and f_0 parameters were fitted using experimental data at 500 mm·min^{-1} (the same extraction speed of 5 mm·min^{-1} was used as described in Section 2.3). Validation at an intermediate speed was therefore performed to assess the model's generality and rate-independence.

Additional virtual cone penetration–extraction tests were conducted at 250 mm·min^{-1}, representing a medium-speed condition between the two experimental speeds (50 and 500 mm·min^{-1}). The same cone geometry, soil container dimensions, and boundary conditions described in Section 2.6 were applied. For each soil texture (three types) and water content (four levels), ten DEM replications were generated with different random seeds to quantify stochastic variability. The average compressive and adhesive forces from simulations were compared with the experimental data obtained at 50 mm·min^{-1} and 500 mm·min^{-1}.

The validation specifically examined whether $\Delta\gamma$-driven compressive behavior and f_0-driven adhesive behavior remained consistent at the intermediate speed.

The validation focused on two key aspects:

(1) Adhesive behavior — examining the predicted maximum tensile (pull-off) forces during extraction to verify that adhesion remained quasi-static and followed the experimentally observed moisture-dependent pattern; and

(2) Compressive behavior — evaluating the peak compressive loads during penetration to confirm that rate-dependent strengthening appeared progressively between low and high speed limits.

Model reliability was quantitatively assessed using multiple statistical metrics including the coefficient of determination (R^2), root mean square error (RMSE), mean absolute error (MAE), and mean absolute percentage error (MAPE). Validation was deemed successful when $R^2 \geq 0.9$, RMSE $\leq$ experimental standard deviation, and MAPE $\leq$ 5%,

combined with visual consistency of the force–displacement curves. Reproduction of both adhesive and compressive trends under the intermediate speed condition was evaluated by comparing simulated and experimental force responses. The DEM-predicted forces closely followed the experimental trends across all soil textures and water contents, maintaining mean relative errors below 5% for compression and 6% for adhesion. These results indicate that the Δγ–f_0 framework maintains comparable predictive performance under intermediate loading rates.

Fig. 10. presents the validation results obtained at an intermediate penetration speed of 250 mm·min^{-1}, which was not used during the calibration stage. As shown in Fig. 10A, the DEM-predicted compressive forces closely follow the experimentally measured values as a function of water content for all three soil textures. The model successfully reproduces both the magnitude and the moisture-dependent trend of compressive resistance, indicating that the surface-energy-driven parameter Δγ calibrated at 500 mm·min^{-1} remains applicable under intermediate loading conditions. Figure 10B compares the corresponding adhesive (pull-off) forces during extraction. Excellent agreement is observed between experimental measurements and DEM predictions across all water contents and soil textures, with mean relative errors remaining below 6%. This result confirms that the pull-off force parameter f_0 consistently governs adhesive behavior and that soil–metal adhesion remains quasi-rate-independent within the investigated penetration-speed range. Together, Fig. 10A and Fig. 10B demonstrate that the calibrated Δγ–f_0 framework accurately reproduces both compressive and adhesive responses at an intermediate penetration speed without additional parameter adjustment, confirming the transferability and robustness of the proposed calibration approach.

3.3.2. *Assessment of DEM Model Performance at the Intermediate Penetration Speed*

To evaluate the predictive capability of the calibrated DEM model under an intermediate penetration rate, a performance assessment was conducted using sandy clay loam at 20% water content. Fig. 11. presents the experimental and DEM-predicted force–time responses obtained at 250 mm·min^{-1}.

The maximum compressive force measured experimentally was 53.79 N, whereas the DEM simulation produced a peak value of 51.78 N, corresponding to a relative error of approximately 3.7%. Similarly, the peak adhesive (pull-off) force during extraction was 1.667 N in the experiment and 1.665 N in the DEM prediction, demonstrating near-identical agreement (<0.2% error). These results show close agreement between experimental and DEM-predicted compressive and adhesive responses at a speed not used during the calibration stage.

Although the experimental soil samples were sieved through a 0.425-mm mesh, the DEM simulations employed spherical particles with a diameter of 10 mm. This coarse-grained representation increases pore space relative to physical soil structure; however, such particle sizes (4–14 mm) are widely adopted in agricultural soil–tool simulations to maintain computational feasibility during large deformation. The objective of this study is to capture macroscopic soil–metal mechanical behavior—penetration resistance and adhesion—rather than to reproduce microscopic soil fabric.

The simulated and measured forces showed close agreement under the intermediate loading condition. The use of coarse-particle DEM beds

was therefore evaluated in terms of their ability to reproduce macroscopic penetration and adhesion forces.

3.4. Statistical Analysis

A two-way ANOVA was conducted to evaluate the effects of soil texture and water content on both compressive and adhesive forces. Both factors were statistically significant ($p < 0.001$), whereas their interaction was not significant ($p > 0.05$). This indicates that the moisture-dependent trends of compressive and adhesive behavior were similar across all soil textures.

During the calibration stage (50 and 500 mm·min^{-1} tests), quadratic regression between water content and force achieved $R^2 \geq 0.93$ and RMSE ≤ 0.1 N across all textures, demonstrating that the DEM model accurately reproduced the experimental trends. Paired t-tests comparing experimental and DEM-predicted forces showed no significant differences ($p > 0.05$), verifying the statistical reliability of the proposed calibration framework.

To further assess predictive reliability, an additional regression analysis was performed for the intermediate speed validation (250 mm·min^{-1}). Coefficients of determination (R^2) between experimental and simulated peak forces were 0.94, 0.93, and 0.97 for compressive behavior and 0.99, 0.996, and 0.99 for adhesive behavior in sandy loam, sandy clay loam, and loam, respectively. All values exceeded 0.93, confirming that

the calibrated $\Delta\gamma$–f_0 framework maintains cross-speed predictive consistency across different soil textures.

Although detailed ANOVA statistics (F-values, effect sizes, and post-hoc comparisons) are not shown for brevity, the analysis confirmed significant main effects of soil texture and water content ($p < 0.001$) and a non-significant interaction ($p > 0.05$). These statistical results indicate that the effects of soil texture and water content on compressive and adhesive behaviors can be evaluated separately within the tested range.

4. Discussions

Building on the statistical results presented in Section 3.4, the absence of a significant texture–moisture interaction can be physically interpreted as follows. This outcome indicates that the effects of soil texture and moisture act independently rather than synergistically, aligning with the quasi-independent mechanisms of $\Delta\gamma$ and f_0 in the EEPA contact model. In this framework, $\Delta\gamma$ primarily governs compressive stiffness through energy stored in elastic–plastic deformation, while f_0 dictates the magnitude of adhesive traction at the soil–metal interface. The lack of statistical interaction between the two factors provides physical evidence that compression- and adhesion-related phenomena are separable processes within the moisture range examined.

Although $\Delta\gamma$ and f_0 are model parameters rather than directly measurable physical quantities, their roles can be interpreted through their influence on experimentally observed force responses. Within the EEPA framework, $\Delta\gamma$ governs the extent of elastic–plastic energy storage

during contact and therefore modulates the compressive resistance measured during penetration, whereas f_0 represents an interfacial pull-off contribution that scales the tensile force observed during extraction. Importantly, the agreement between simulated and measured force trends does not imply a direct physical correspondence between these parameters and measurable soil properties. Instead, it indicates that $\Delta\gamma$ and f_0 act as effective model parameters that capture distinct aspects of the penetration–extraction response within the EEPA contact formulation.

It should be noted that the present DEM framework was designed to reproduce macroscopic soil–metal force responses rather than to resolve microscopic contact-level mechanics. The soil bed was represented using coarse-grained spherical particles to ensure computational efficiency under large deformation. Under this modeling approach, the absolute number of particle–cone contacts is strongly dependent on particle size, packing configuration, and numerical coarse-graining strategy, and therefore does not directly correspond to a physically meaningful contact count in real soil.

Nevertheless, even though the absolute number of particle–cone contacts is model-dependent under coarse-grained DEM representations, the spatial distribution of contacts around the cone plays an important role in determining the macroscopic force response. During penetration and extraction, the cone simultaneously interacts with multiple particles, forming a distributed contact network that governs load transfer and

adhesive force development at the soil–metal interface. Therefore, while the present study does not analyze contact statistics explicitly, the macroscopic compressive and pull-off force responses implicitly reflect the collective behavior of these particle–cone interactions.

As a result, reporting the number of particle–cone contacts would not provide a quantitatively transferable micromechanical interpretation of adhesion force magnitude. Instead, adhesion formation is implicitly captured through the combined effects of contact area evolution, elastic–plastic deformation, and EEPA-based adhesive interactions, which are reflected in the experimentally measurable compressive and pull-off force responses. A detailed micromechanical analysis based on contact statistics is beyond the scope of the present study and remains an important topic for future work using finer particle resolutions or multiscale modeling approaches.

Increased water content enhanced both compressive and adhesive forces up to approximately 20–25%, beyond which adhesion declined. This moisture threshold corresponds to the transition between the plastic and liquid limits determined from Atterberg testing, where capillary bridge cohesion and liquid-film lubrication coexist. Similar trends have been reported in previous experimental works on clayey and loamy[18-21,13], supporting the interpretation that adhesion peaks near the liquid limit due to optimal water-film thickness and contact area. The DEM calibration reproduced this trend accurately by linking $\Delta\gamma$ monotonically with water content, suggesting that $\Delta\gamma$ effectively represents the

contribution of capillary cohesion and particle–particle bonding to overall adhesion.

The quasi-static behavior of adhesive force with respect to penetration rate also has notable implications. Despite a three-fold increase in compressive resistance when penetration speed rose from 50 to 500 mm·min^{-1}, adhesion changed by less than 5%. This indicates that adhesive forces are dominated by surface energy and interfacial bonding rather than dynamic inertia or viscous damping. Consequently, high-speed testing can substantially improve experimental efficiency without compromising the physical accuracy of adhesion measurements. This finding supports the use of 500 mm·min^{-1} as the reference speed for DEM calibration and suggests that adhesion can be considered approximately rate-independent within the quasi-static penetration-speed range examined in this study.

Statistical testing supported the main effects of soil texture and water content and a non-significant interaction, providing a basis for the subsequent physical interpretation. Beyond verification, the $\Delta\gamma$–f_0 calibration framework offers practical advantages for modeling soil–tool and soil–tire interactions in agricultural machinery. Since $\Delta\gamma$ and f_0 can be independently tuned to represent compressive and adhesive responses, the model can flexibly adapt to different soil types, moisture regimes, or surface materials without reparameterization of the entire contact law. This feature allows the same DEM bed to simulate diverse implement operations, such as tillage, digging, or garlic harvesting, while

maintaining consistent physical behavior. The validated high-speed experimental methodology also provides a scalable reference for field-level applications where dynamic interactions dominate.

Overall, this study establishes a unified and physically interpretable framework for analyzing soil–metal adhesion under controlled laboratory conditions. By decoupling surface-energy-driven and pull-off-force-driven mechanisms, the proposed $\Delta\gamma$–f_0 calibration strategy provides a robust basis for reproducing experimentally observed compressive and adhesive force trends within the tested penetration-speed range.

It should be noted that the present study focused exclusively on soil–metal interactions, and soil–rubber adhesion was not experimentally investigated. Therefore, extension of the proposed framework to soil–tire or traction-related applications requires additional experimental validation and model refinement. Moreover, the penetration speeds examined in this study were lower than typical field tillage velocities; consequently, direct applicability to full-scale field operations should be interpreted with caution.

Nevertheless, the methodology developed here offers a physically grounded and computationally efficient reference for DEM-based soil adhesion modeling, and can inform future studies aimed at tool design optimization and soil–machine interaction analysis under broader operating conditions.

Although the cone surface roughness was quantitatively characterized in this study, the independent influence of surface

roughness on soil adhesion was not systematically investigated. Therefore, the results should be interpreted as representing soil–metal adhesion behavior under the specific surface condition of the cone used in the present experiments.

5. Conclusions

This study examined the influence of soil texture and water content on soil–metal adhesion through high-speed experiments and discrete element method (DEM) simulations based on the Edinburgh Elasto-Plastic Adhesion (EEPA) model. Three soil textures—sandy loam, sandy clay loam, and loam—were tested under water contents ranging from 10 to 25%, using a stainless-steel cone to measure both compressive and adhesive forces. The results revealed that adhesion increased with water content and reached its maximum near the liquid limit (20–25%), beyond which lubrication effects caused a gradual decline.

$\Delta\gamma$ and f_0 were identified as the principal parameters controlling soil mechanical response. $\Delta\gamma$ governed compressive stiffness through inter-particle bonding and capillary cohesion, whereas f_0 determined adhesive traction at the soil–metal interface. The two parameters acted quasi-independently, as confirmed by two-way ANOVA results, which showed no significant interaction between texture and water content ($p > 0.05$). This independence validates the physical interpretation that compressive and adhesive mechanisms are separable within the EEPA framework.

High-speed testing at 500 mm·min^{-1} proved effective for adhesion measurement, yielding comparable results to conventional low-speed tests while significantly improving experimental throughput. The weak rate sensitivity of adhesion (<5% variation between 50 and 500 mm·min^{-1}) indicates that adhesion is dominated by surface energy and contact bonding rather than viscous effects. Consequently, high-speed calibration can serve as a practical and time-efficient alternative for large experimental datasets and DEM model development.

Statistical analyses further verified the reliability of the calibrated model, achieving $R^2 \geq 0.93$ and RMSE $\leq$ 0.1 N across all textures, with no significant difference ($p > 0.05$) between experimental and DEM-predicted adhesion. The validated $\Delta\gamma$–f_0 framework successfully reproduced both compressive and adhesive behaviors across varying moisture conditions and penetration rates, confirming its robustness under the tested conditions.

Cross-speed validation at 250 mm·min^{-1} further verified the model's predictive consistency ($R^2 \geq 0.93$, RMSE $\leq$ 0.1 N) across all textures, demonstrating that parameters calibrated at high speed remain stable under intermediate loading conditions. Overall, this study establishes a unified, physically interpretable approach for analyzing soil adhesion. By decoupling surface-energy-driven and pull-off-force-driven mechanisms, the proposed calibration strategy provides a reliable basis for predicting soil–tool and soil–tire interactions under the tested soil texture and

moisture conditions. The methodology and findings can potentially be extended to the design optimization of tillage implements, harvesting tools, and traction systems operating in cohesive soils.

The applicability of the present findings should be interpreted within the investigated range of soil textures and moisture contents. This study focused on sandy loam, sandy clay loam, and loam soils at water contents of 10–25%, corresponding to plastic to near-liquid consistency states where soil–metal adhesion is experimentally stable and practically relevant for many agricultural operations. More extreme soil conditions were not considered. Highly cohesive heavy clays near saturation may exhibit pronounced undrained behavior and large-scale structural deformation, whereas very coarse soils such as pure sands may show negligible adhesion governed by fundamentally different contact mechanics. Extending the proposed framework to such conditions would require additional experimental protocols and modeling considerations, including drainage-dependent behavior and alternative contact formulations. These aspects will be addressed in future studies to further evaluate the generality of the proposed DEM calibration framework.

By integrating multi-speed experimental adhesion measurements with EEPA-based DEM calibration, this study establishes a physically grounded framework for modeling soil adhesion experimentally validated soil texture and moisture conditions. The resulting $\Delta\gamma$–f_0 parameterization can be applied to DEM–MBD coupling models to improve predictions of PTO power requirements, draft forces, traction

performance, soil–tool contact stresses, and clogging tendencies in cohesive soils[13,14,16,36]. Ultimately, this framework supports the design and optimization of agricultural machinery operating across diverse field environments.

Acknowledgements

This study was funded by the Ministry of Agriculture, Food and Rural Affairs, supported by the Korea Institute of Planning and Evaluation for Technology in Food, Agriculture and Forestry (IPET)'s Upland Agricultural Mechanization Promotion Technology Development Project (RS-2023-00236042).

Funding declaration

This work was supported by the Ministry of Agriculture, Food and Rural Affairs (MAFRA), through the Korea Institute of Planning and Evaluation for Technology in Food, Agriculture and Forestry (IPET), under the Upland Agricultural Mechanization Promotion Technology Development Project (RS-2023-00236042), the International Cooperation-based Export Agricultural Competitiveness Enhancement Technology Development Project (RS-2023-00233191), and the Offload Smart Agricultural Utilization Model Development Project (RS-2025-02313136).

Data availability

All data generated or analyzed during this study are included in this published article.

References

[1] McKyes, E. Soil Cutting and Tillage. (Elsevier, Amsterdam, 1985).

[2] Srivastava, A. K., Goering, C. E. & Rohrbach, R. P. *Engineering Principles of Agricultural Machines*. (ASABE, St. Joseph, MI, 2006).

[3] Zoz, F. M. & Grisso, R. D. Traction and tractor performance. *ASABE Monogr.* (ASABE, St. Joseph, MI, 2003).

[4] Balsari, P. et al. Performance analysis of a tractor–power harrow system under different working conditions. *Biosyst. Eng.* **202**, 28–41 (2021).

[5] Czarnecki, J. et al. Analysis of traction properties and power of wheels used on various agricultural soils. *Agric. Eng.* **23**, 13–23 (2019).

[6] Kim, W. S. et al. Analysis of the load distribution and contact safety factor of PTO gears of a 71 kW class agricultural tractor. *Agriculture* **10**, 2073 (2020).

[7] Tekeste, M. Z. et al. Discrete element modeling of cultivator sweep-to-soil interaction. *J. Terramech.* **82**, 1–11 (2019).

[8] Kešner, Z. et al. Stress distribution on a soil tillage machine frame segment with a chisel shank simulated using DEM and FEM. *Biosyst. Eng.* **209**, 125–138 (2021).

[9] Du, J. et al. Investigation of the burial and mixing performance of a rotary tiller using the discrete element method. *Soil Tillage Res.* **220**, 105349 (2022).

[10] Sun, J. et al. DEM simulation of bionic subsoilers with drag reduction. *Adv. Eng. Softw.* **119**, 30–37 (2018).

[11] Zhao, H. et al. Applications of DEM in agricultural machinery: a review. *Agriculture* **11**, 504 (2021).

[12] Aikins, K. A. et al. Review of discrete element method simulations of soil tillage and furrow opening. *Agriculture* **13**, 541 (2023).

[13] Kim, Y. S. et al. DEM simulation for draft force prediction of moldboard plow according to tillage depth in cohesive soil. *Comput. Electron. Agric.* **189**, 106368 (2021).

[14] Bae, B. M. et al. Prediction of draft force of moldboard plow according to travel speed in cohesive soil using the discrete element method. *Agronomy* **13**, 2073 (2023).

[15] Bae, B. M. et al. Effect analysis of tillage depth on rotavator shaft load using the discrete element method. *Agronomy* **13**, 1229 (2023).

[16] Bae, B. M. et al. Simulation study on draft force prediction of moldboard plow according to cohesive soil particle size using DEM. *Agronomy* **14**, 2205 (2024).

[17] Wang, X. et al. Effect of soil particle-size distribution on soil–subsoiler interactions in DEM. *Span. J. Agric. Res.* **19**, e01 (2021).

[18] Abbaspour-Gilandeh, Y. et al. Investigation of the effect of soil moisture content, contact surface material and soil texture on soil friction and soil adhesion coefficients. *Acta Technol. Agric.* **21**, 44–50 (2018).

[19] Li, H. et al. Correlation between soil structural parameters and soil adhesion based on water film theory. *Coatings* **12**, 1743 (2022).

[20] Li, J. et al. Investigating soil adhesion and anti-adhesion performance of nonsmooth subsoiler surfaces. *J. Eng.* **2024**, 7019756 (2024).

[21] Salem, S. et al. Effect of biomimetic surface geometry, soil texture, and tillage speed on soil–tool adhesion. *Appl. Sci.* **11**, 8927 (2021).

[22] Marigo, J. J. & Stitt, E. H. Discrete element method for cohesive granular materials: Modelling and validation. *Powder Technol.* **200**, 1–15 (2015).

[23] Ditzler, C., Scheffe, K. & Monger, H. C. *USDA Handbook 18: Soil Survey Manual*. (Government Printing Office, Washington, DC, 2017).

[24] Flint, A. L. & Flint, L. E. Particle density. In *Methods of Soil Analysis, Part 4: Physical Methods* 229–240 (SSSA, Madison, 2002).

[25] Qiu, T. & Zhang, Y. Experimental research on the adhesion characteristics of clay to structures with different materials. *Geofluids* **2021**, 3794889 (2021).

[26] Morrissey, J. P., Thakur, S. C. & Ooi, J. Y. EDEM contact model: adhesive elasto-plastic model. *Granul. Matter* **16**, 383–400 (2014).

[27] Yerro, A. & Ceccato, F. Soil–water–structure interactions. *Geotechnics* **3**, 301–305 (2023).

[28] Korean Standards Association. KS F 2303: Test method for liquid limit and plastic limit of soils (2018).

[29] Jeong, D. W. et al. Effect of soil texture and water content on the soil–material adhesion force. *Precis. Agric. Sci. Technol.* **7**, 103–113 (2025).

[30] ISO 1302. Geometrical product specifications (GPS)—Indication of surface texture. (International Organization for Standardization, Geneva, 2002).

[31] Whitehouse, D. J. *Handbook of Surface Metrology*. 2nd ed. (CRC Press, Boca Raton, FL, 2011).

[32] Liu, G. et al. Research on an intelligent vibration detachment system for rotary tiller based on soil surface roughness dynamic characteristics. *Comput. Electron. Agric.* **224**, 109214 (2024)

[33] Kim, Y. S. et al. Prediction of PTO power requirements according to surface energy during rotary tillage using a DEM–MBD coupling model. *Agronomy* **14**, 10679 (2024).

[34] Bae, B. M. et al. Development of a power prediction model for rotary tillage in paddy loam field using DEM–MBD coupling method. *J. Terramech.* (in press) (2025).

[35] Thakur, S. C., Morrissey, J. P. & Ooi, J. Y. A cohesive granular model with tunable stress history dependence. *Granul. Matter* **16**, 383–400 (2014).

[36] Choi, S. O. et al. Analysis of PTO shaft loads and power requirements for a tractor-attached garlic harvester. *J. Agric. Mach. Eng.* **5**, 1–12 (2025).

[37] Coetzee, C. J. Calibration of the discrete element method and the effect of particle shape. *Powder Technol.* **297**, 50–70 (2016).

[38] Zhang, Q. & Kushwaha, R. L. Soil–tool interaction: A review and an experimental analysis. *J. Terramech.* **36**, 111–123 (1999).

[39] Coetzee, C. J. & Els, D. P. Calibration of discrete element parameters and modelling of silo discharge and bucket filling. *Comput. Electron. Agric.* **65**, 198–212 (2009).

[40] Liu, Z. et al. DEM simulation of soil flow in tillage tools. *Biosyst. Eng.* **141**, 1–13 (2016).

[41] Iwashita, K. & Oda, M. Rolling resistance at contacts in simulation of shear band development by DEM. *Powder Technol.* **109**, 192–199 (1998).

[42] Ai, J. et al. Assessment of rolling resistance models in discrete element simulations. *Powder Technol.* **206**, 269–282 (2011).

[43] Zhao, J., Guo, N. & Utili, S. DEM analysis of granular soils with rolling resistance. *Granul. Matter* **19**, 1–15 (2017).

[44] Tsuji, Y., Tanaka, T. & Ishida, T. Lagrangian numerical simulation of plug flow of cohesionless particles in a horizontal pipe. *Powder Technol.* **71**, 239–250 (1992).

[45] Gao, J. et al. Mechanical properties of clayey soils and DEM calibration. *Soil Tillage Res.* **155**, 1–10 (2014).

[46] Zhang, Z. et al. DEM analysis of granular soils with rolling resistance. *Granul. Matter* **19**, 1–15 (2017).

[47] Gao, J. et al. Mechanical behavior of cohesive soils under DEM calibration. *Soil Tillage Res.* **158**, 1–10 (2016).

[48] Ucgul, M., Fielke, J. M. & Saunders, C. Discrete element modelling of tillage forces and soil movement. *Soil Tillage Res.* **148**, 22–33 (2015).

[49] Brilliantov, N. V. et al. Model for collisions in granular gases. *Phys. Rev. E* **53**, 5382–5392 (1996).

[50] Cundall, P. A. & Strack, O. D. L. A discrete numerical model for granular assemblies. *Géotechnique* **29**, 47–65 (1979).

Fig. 1. Field test site and soil measurement procedures.

Table 1

Soil texture and Atterberg Limits by Field

Soil analysis	Field A	Field B	Field C
Field location	Taean-gun, Chungcheongnam-do (36°45'15.4"N 126°12'58.7"E)	Miryang-si, Gyeongsangnam-do (35°30'08.5"N 128°43'19.9"E)	Miryang-si, Gyeongsangnam-do (35°30'08.3"N 128°43'18.7"E)
Sand	73.8%	52%	50%
Silt	11.8%	26%	28%
Clay	14.4%	22%	22%
Soil texture	Sandy loam	Sandy clay loam	Loam
Plastic limit	9.282%	15.281%	16.495%
Liquid limit	25.723%	27.723%	27.790%
Plastic index	16.441%	12.442%	11.295%

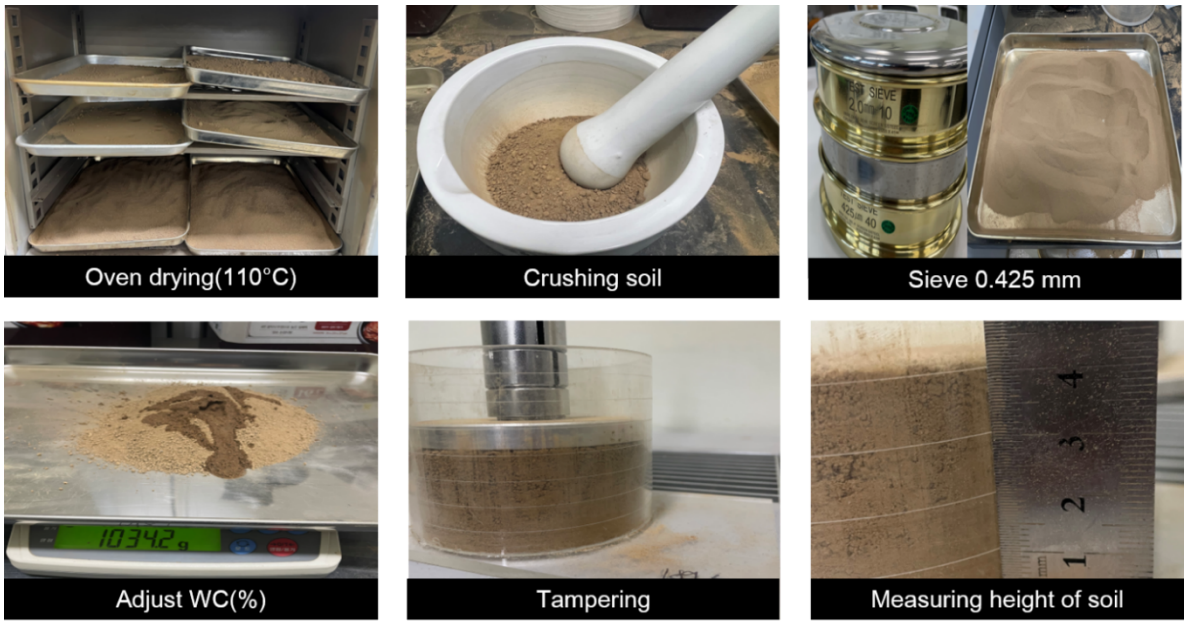

Fig. 2. Preparation of soil samples for measuring adhesion

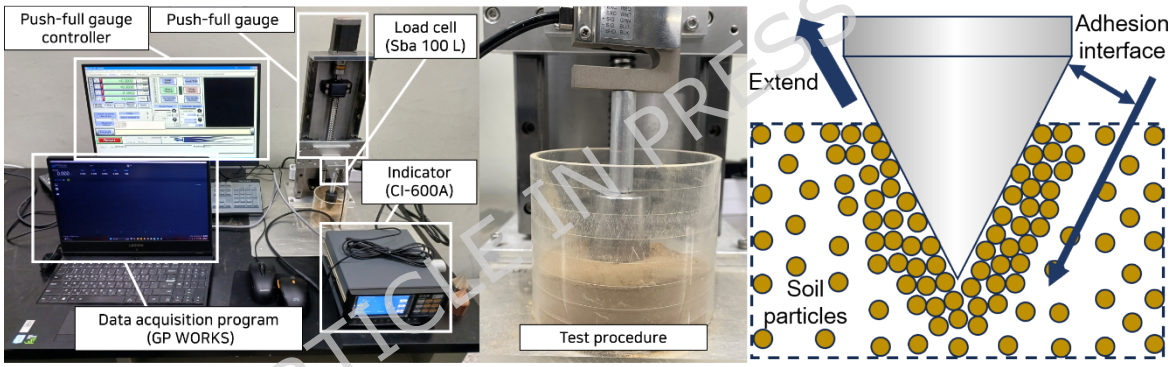

Fig. 3 Experimental setup and measurement principle for soil–metal adhesive force tests.

(A) Overall configuration of the test system, including the push–pull gauge controller, load cell, indicator, and data acquisition program.

(B) Cone penetration–extraction test procedure conducted using a stainless-steel cone in a soil-filled container.

(C) Schematic illustration of the cone–soil interaction during penetration and extraction, highlighting the adhesion interface governing the measured pull-off force.

Table 2

Specifications of data acquisition system for measuring adhesive force.

Item	Specification
Indicator	CI-600A
Data acquisition program	GP WORKS
Capacity	100 kgf (≈ 981 N)
Resolution	20 gf (≈ 0.196 N)
Allowable overload	150 kgf (≈ 1471 N)

Table 3

Cone tip specifications

Test cone	Steel
Structural materials	SS401
Generatrix	35 mm
Top angle	54.4°
Cylinder diameter	32 mm
Cylinder height	30 mm
Cone area	$1.649 * 10^{-3} m^2$
Surface roughness (Ra)	0.85 ± 0.13 μm

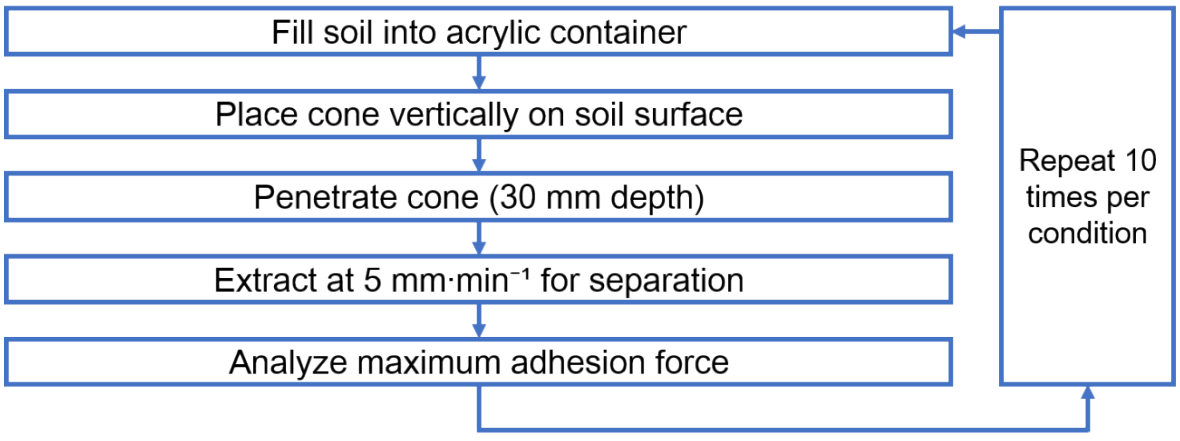

Fig. 4. Experimental Method for Soil adhesive force

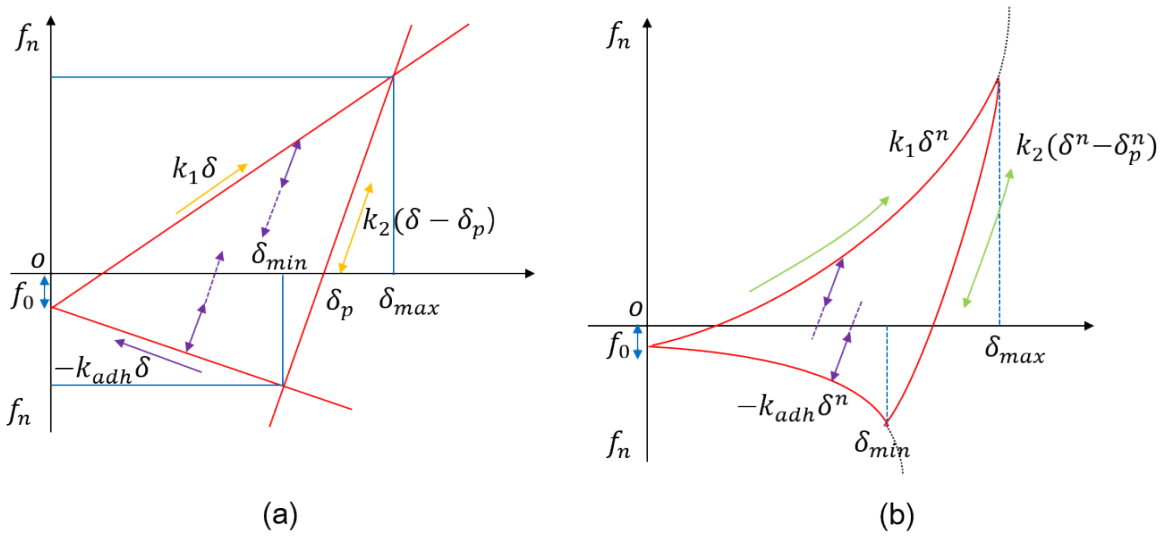

Fig. 5. EEPA model normal contact force–displacement relationship: (a) linear and (b) non-linear(schematic redrawn by the authors based on reported EEPA formulation[26]).

Table 4

Parameters of the EEPA contact model

Parameter	Description	Unit	Role in model
k_1	Loading stiffness	N/m^n	Governs initial loading force
$k_2 = \lambda_p k_1$	Unloading/reloading stiffness	N/m^n	Defines hysteresis (plasticity ratio)
n	Stiffness exponent	–	Controls nonlinearity
f_0	Constant pull-off force	N	Represents van der Waals adhesion
$\Delta\gamma$	Surface energy	J/m^2	Calibrated to match adhesion
k_{adh}	Adhesive stiffness parameter	N/m^x	Governs adhesion growth
δ_p	Plastic overlap	m	Threshold for permanent deformation
X	Adhesion power value	–	Shapes adhesion- overlap curve
k_t	Tangential stiffness	N/m	Defines shear stiffness
c_t	Tangential damping coefficient	Ns /m	Controls tangential damping
μ	Static friction coefficient	–	Limits tangential force
μ_r	Rolling resistance coefficient	–	Defines rolling torque

c_n	Normal damping coefficient	Ns /m	Dissipates impact energy

Table 5

Modeling parameters of particle contact model in the DEM software.

Parameter	Value	Source
Surface energy	Calibrated	Calibrated in this study
Constant pull-off force	Calibrated	Calibrated in this study
Tensile exponent	5	[34]
Tangential stiff multiplier	0.28571	[34]
Slope exponent	1.5	[34]
Contact plastic ratio	0.75	[34]

Table 6

DEM soil modeling parameters for sandy loam soil used in this study

Parameter	Value	Source
Particle size	Radii 5 mm	Present study
Poisson’s ratio of soil	0.32	[37], [46]
Poisson’s ratio of steel	0.3	[34]
Static friction coefficient of soil-soil	0.81	[1], [38]
Static friction coefficient of soil-steel	0.85	[1], [38]
Rolling friction coefficient of soil-soil	0.29	[41], [42]
Rolling friction coefficient of soil-steel	0.23	[42], [43]
Coefficient of restitution of soil-soil	0.45	[44], [37]
Coefficient of restitution of soil-steel	0.35	[44]

Table 7

DEM soil modeling parameters adopted for sandy clay loam and loam soils treated as cohesive soils

Parameter	Value	Source
Particle size	Radii 5 mm	Present study
Poisson’s ratio of soil	0.32	[45], [46]
Poisson’s ratio of steel	0.3	[34]

Static friction coefficient of soil-soil	0.36	[1], [47]
Static friction coefficient of soil-steel	0.24	[38], [1]
Rolling friction coefficient of soil-soil	0.18	[41], [42]
Rolling friction coefficient of soil-steel	0.12	[42], [48]
Coefficient of restitution of soil-soil	0.30	[44], [49]
Coefficient of restitution of soil-steel	0.40	[50], [44]

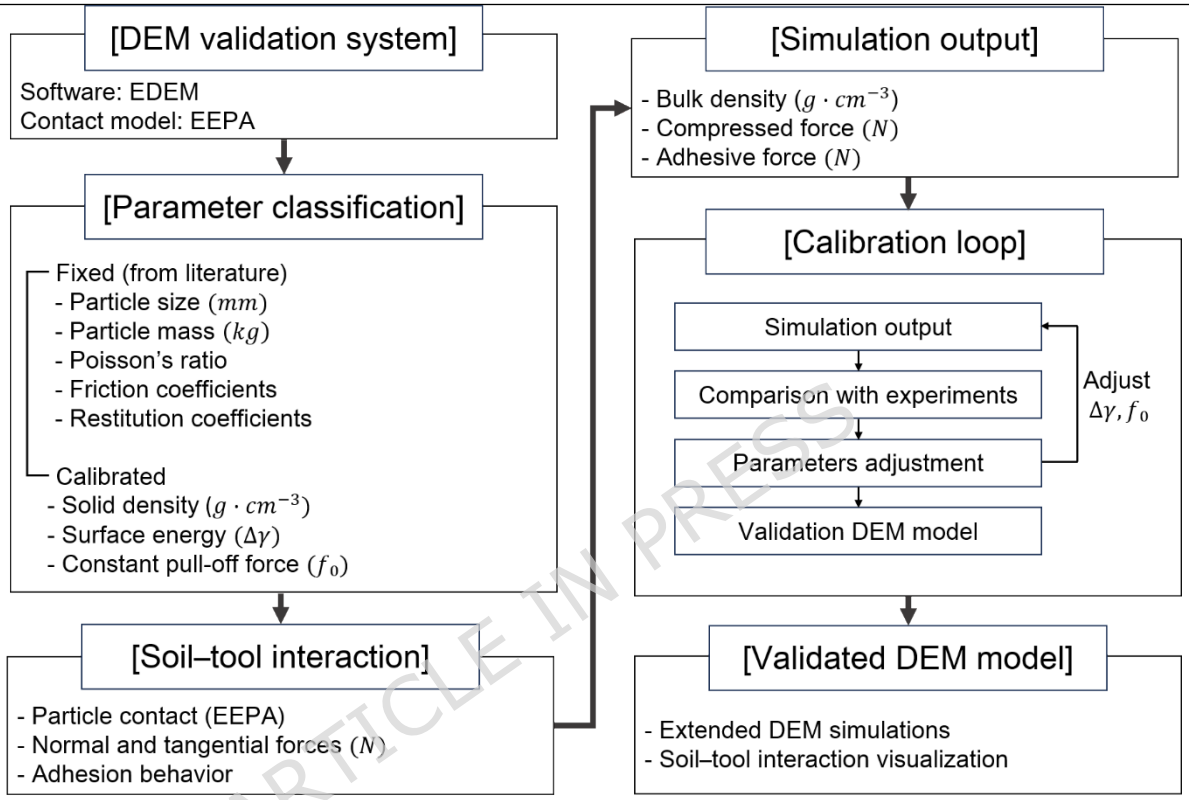

Fig. 6. Calibration and validation workflow using DEM

Table 8

Dry bulk density of sandy loam, sandy clay loam, and loam soils under different water contents (10–25%, dry basis).

Soil texture	Water content (%)	Dry soil mass (g)	Water mass (g)	Soil height (cm)	Wet bulk density (g·cm^{-3})	Bulk density (g·cm^{-3})
Sandy loam	10	314.37	31.44	4.34	1.3 ± 0.08	1.18 ± 0.08
	15	317.09	47.56	4.33	1.35 ± 0.11	1.17 ± 0.09
	20	321.48	64.3	3.95	1.54 ± 0.07	1.29 ± 0.06
	25	337.34	84.34	3.97	1.64 ± 0.13	1.31 ± 0.11
Sandy clay loam	10	259.79	25.98	4.01	1.16 ± 0.06	1.06 ± 0.05
	15	289.55	43.43	4.09	1.31 ± 0.12	1.14 ± 0.1
	20	289.77	57.95	3.59	1.53 ± 0.15	1.27 ± 0.12
	25	283.82	70.95	3.12	1.75 ± 0.11	1.4 ± 0.09

Loam	10	269.68	26.97	4.05	1.19 ± 0.07	1.08 ± 0.06
	15	271.87	40.78	4.15	1.21 ± 0.09	1.05 ± 0.08
	20	275.8	55.16	3.69	1.42 ± 0.09	1.18 ± 0.08
	25	276.9	69.22	3.07	1.74 ± 0.08	1.39 ± 0.06

Table 9

Calibration results of bulk density

Soil texture	Water content (%)	Particle mass (□g)	Bulk density (g·cm^{-3})		Calibration error (%)
			Simulated	Measured	
Sandy loam	10	0.00143161	1.178	1.18 ± 0.08	0.169
	15	0.0014228	1.172	1.17 ± 0.09	0.171
	20	0.00155341	1.278	1.29 ± 0.06	0.930
	25	0.0015775	1.311	1.31 ± 0.11	0.085
Sandy clay loam	10	0.00127645	1.053	1.06 ± 0.05	0.661
	15	0.00137278	1.138	1.14 ± 0.1	0.351
	20	0.00152933	1.278	1.27 ± 0.12	0.630
	25	0.00168588	1.409	1.4 ± 0.09	0.643
Loam	10	0.00130053	1.073	1.08 ± 0.06	0.648
	15	0.00126441	1.044	1.05 ± 0.08	0.571
	20	0.00142095	1.188	1.18 ± 0.08	0.678
	25	0.00167384	1.397	1.39 ± 0.06	0.6

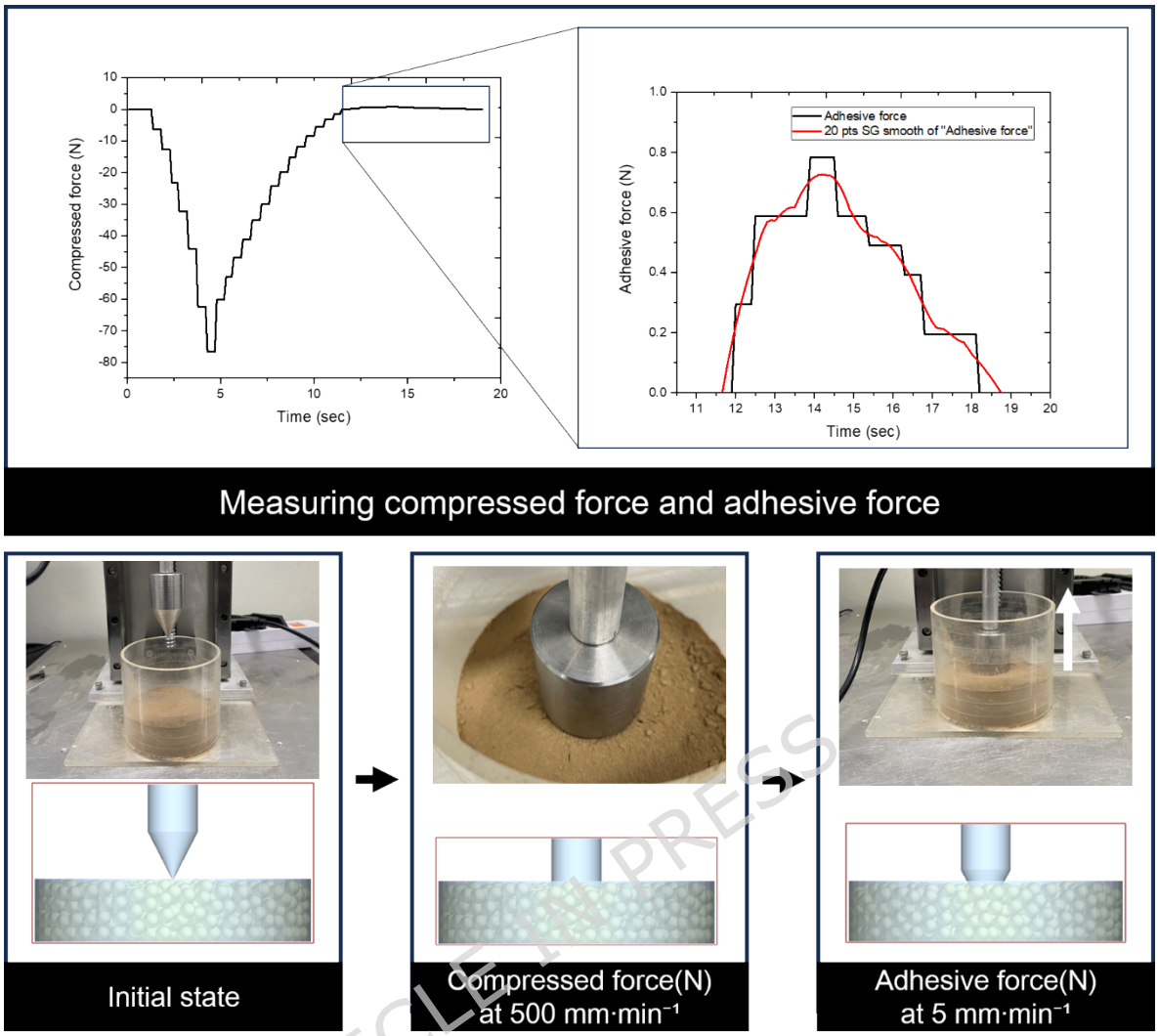

Fig. 7. Comparison between experimental and EDEM-predicted adhesive forces for model calibration using the EEPA contact model.

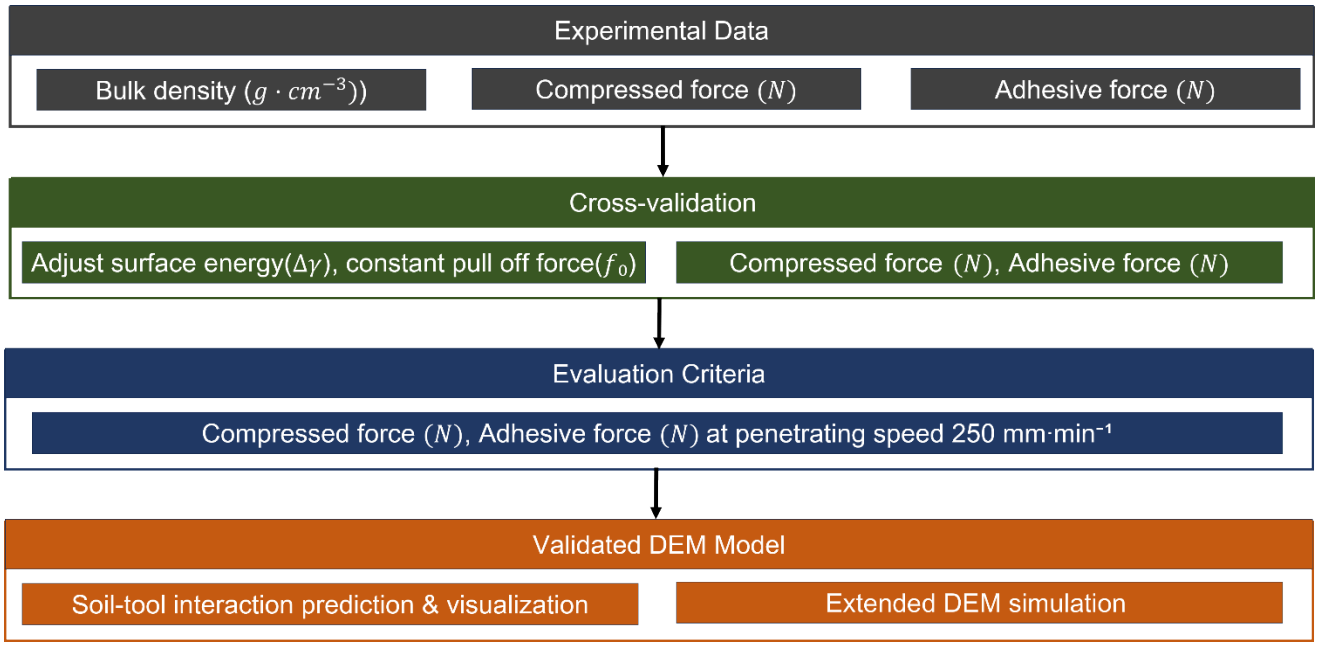

Fig. 8. Overall flow chart of soil adhesive force prediction model

Table 10

Compressive and adhesive forces of sandy loam, sandy clay loam, and loam soils at a penetration speed of 500 mm·min⁻¹ (extraction speed of 5 mm·min⁻¹).

Soil texture	Water content (%)	Compressed force (N)	Adhesive force (N)
Sandy loam	10	47.269	0.196
	15	77.279	1.275
	20	74.141	1.765
	25	50.212	1.471
Sandy clay loam	10	47.466	0.098
	15	76.691	0.785
	20	65.119	1.765
	25	34.423	1.961
Loam	10	39.228	0.098
	15	74.337	0.883
	20	72.768	1.765
	25	43.347	2.158

Table 11

Compressive and adhesive forces of sandy loam, sandy clay loam, and

loam soils at a penetration speed of 50 mm·min^{-1} (extraction 5 mm·min^{-1}).

Soil texture	Water content (%)	Compressed force (N)	Adhesive force (N)
Sandy loam	10	35.011	0.172
	15	49.329	1.138
	20	45.112	1.785
	25	21.575	1.451
Sandy clay loam	10	27.165	0.098
	15	42.660	0.824
	20	25.890	1.785
	25	22.948	2.039
Loam	10	32.657	0.089
	15	49.133	1.147
	20	27.852	1.834
	25	23.426	2.216

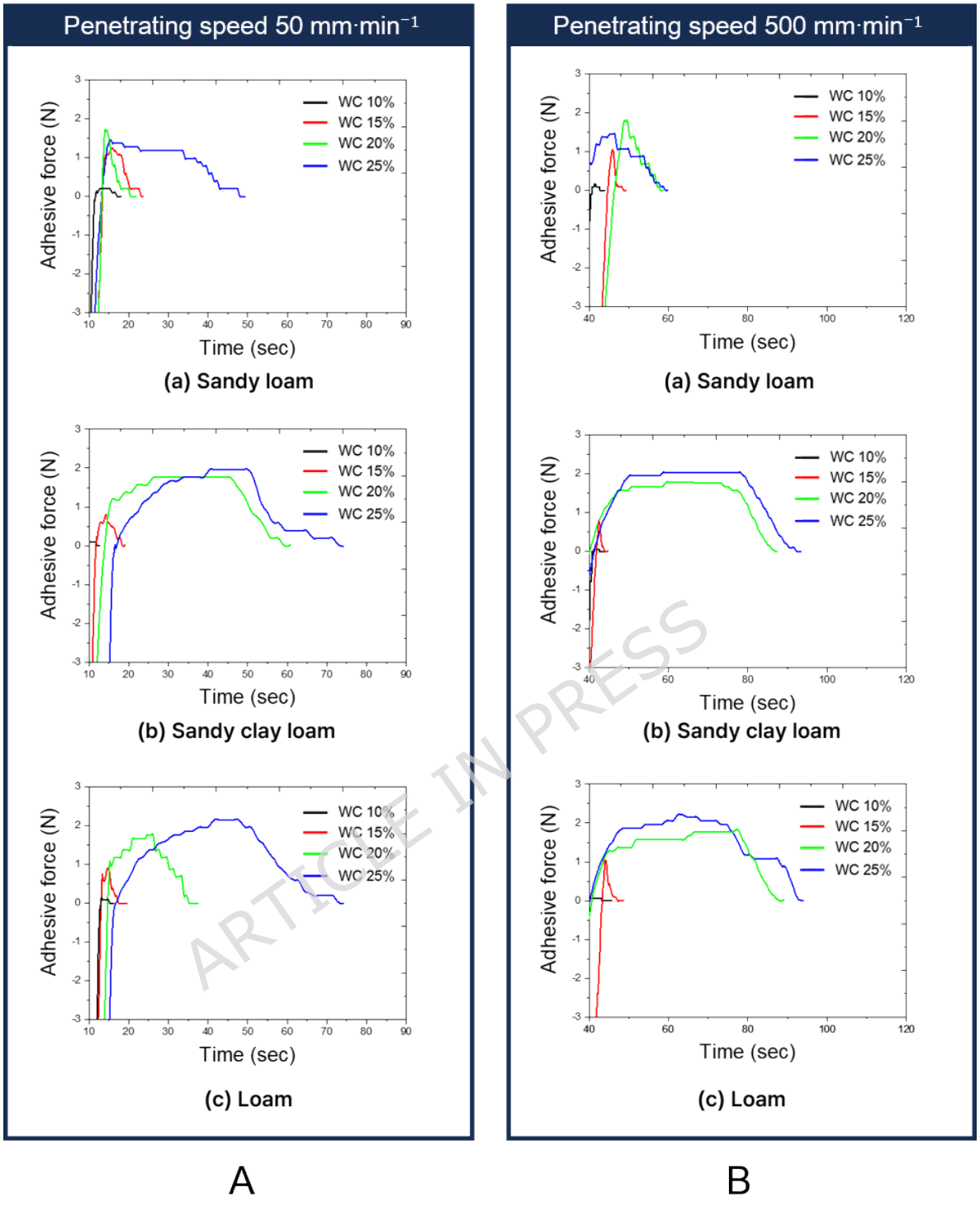

Fig. 9. Typical force–displacement curves of stainless-steel cone penetration tests under different penetration speeds.

(A) Penetration speed of 500 mm·min^{-1}, showing increased compressive resistance.

(B) Penetration speed of 50 mm·min⁻¹, representing quasi-static loading conditions.

In each panel, subplots (a–c) correspond to sandy loam, sandy clay loam, and loam soils, respectively.

Table 12

Surface-energy-based calibration of compressive force by soil texture and water content.

Soil texture	Water content (%)	Calibrated ($\Delta\gamma$, $J_{\bullet}m^{-1}$)	Compressed force (Exp)	Compressed force (DEM)	Abs. error	Rel. error (%)
Sandy loam	10	12	47.269	49.690	2.421	5.122
	15	16	77.279	72.559	4.720	6.108
	20	15	74.141	73.956	0.185	0.250
	25	9	50.212	49.277	0.935	1.862
Sandy clay loam	10	10	47.466	48.176	0.710	1.496
	15	17	76.691	73.332	3.359	4.380
	20	16	65.119	70.126	5.007	7.689
	25	9	34.423	36.172	1.749	5.081
Loam	10	14	39.228	42.003	2.775	7.074
	15	18	74.337	73.456	0.881	1.185
	20	17	72.768	72.670	0.098	0.135
	25	11	43.347	46.638	3.291	7.592

Table 13

Pull-off-force-based calibration of adhesive force by soil texture and water content.

Soil texture	Water content (%)	Calibrated (f_0)	Adhesion (Exp)	Adhesion (DEM)	Abs. error	Rel. error (%)
Sandy loam	10	-0.02	0.196	0.184	0.012	6.122
	15	-0.05	1.275	1.373	0.098	7.686
	20	-0.09	1.765	1.672	0.093	5.270
	25	-0.07	1.471	1.506	0.035	2.380
Sandy clay loam	10	-0.01	0.098	0.096	0.002	2.041
	15	-0.04	0.785	0.883	0.098	7.686
	20	-0.11	1.961	1.895	0.066	3.366
	25	-0.09	1.863	1.696	0.167	8.963
Loam	10	-0.01	0.098	0.091	0.007	7.143
	15	-0.05	0.883	0.824	0.059	6.681
	20	-0.1	1.765	1.642	0.123	6.972

	25	-0.12	2.158	2.247	0.089	4.123

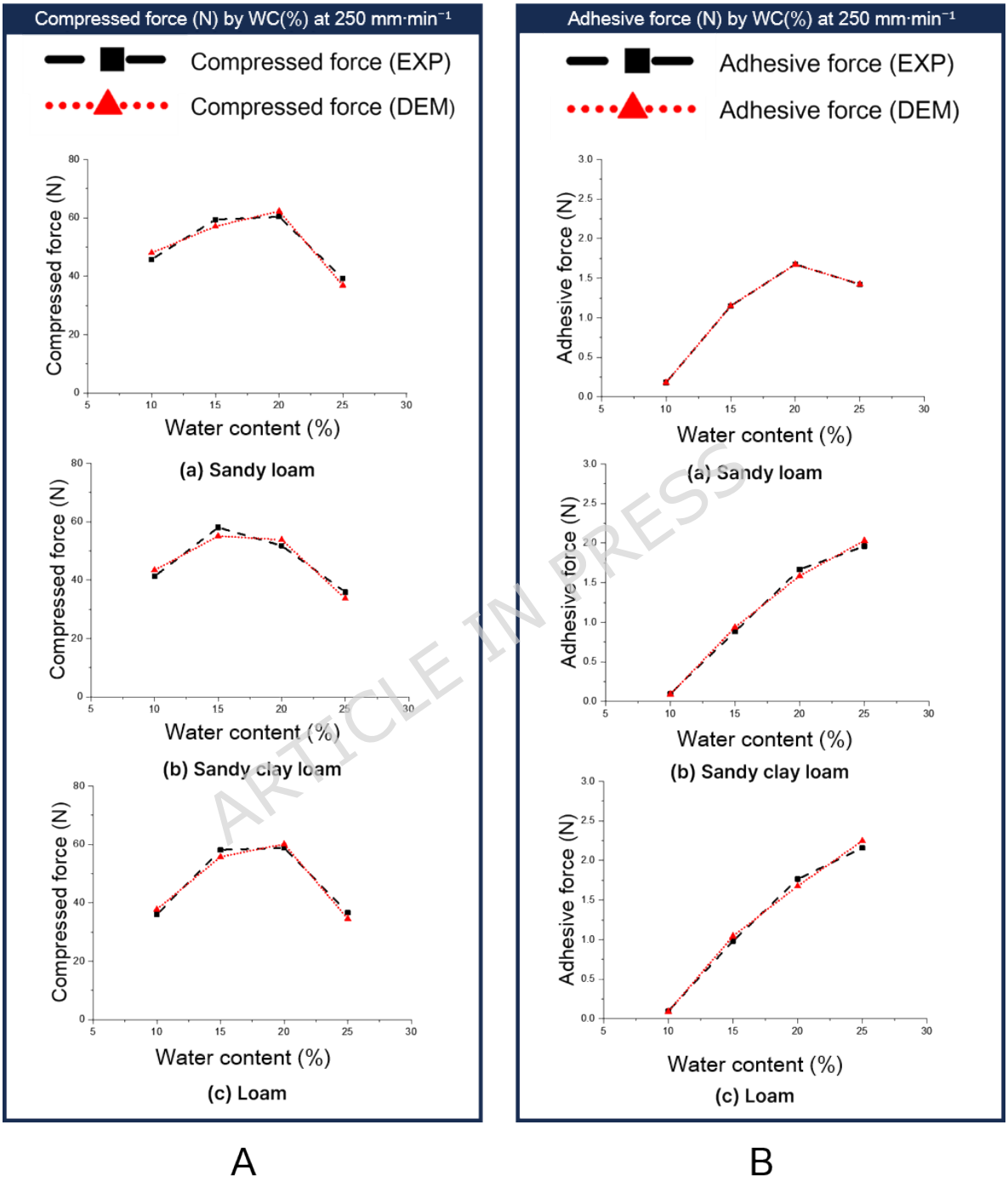

Fig. 10. Validation of DEM predictions at an intermediate penetration speed of 250 mm·min⁻¹.

(A) Comparison of experimental and DEM-predicted compressive forces as a function of water content.

(B) Comparison of experimental and DEM-predicted adhesive forces as a function of water content.

In each panel, results are shown separately for sandy loam, sandy clay loam, and loam soils.

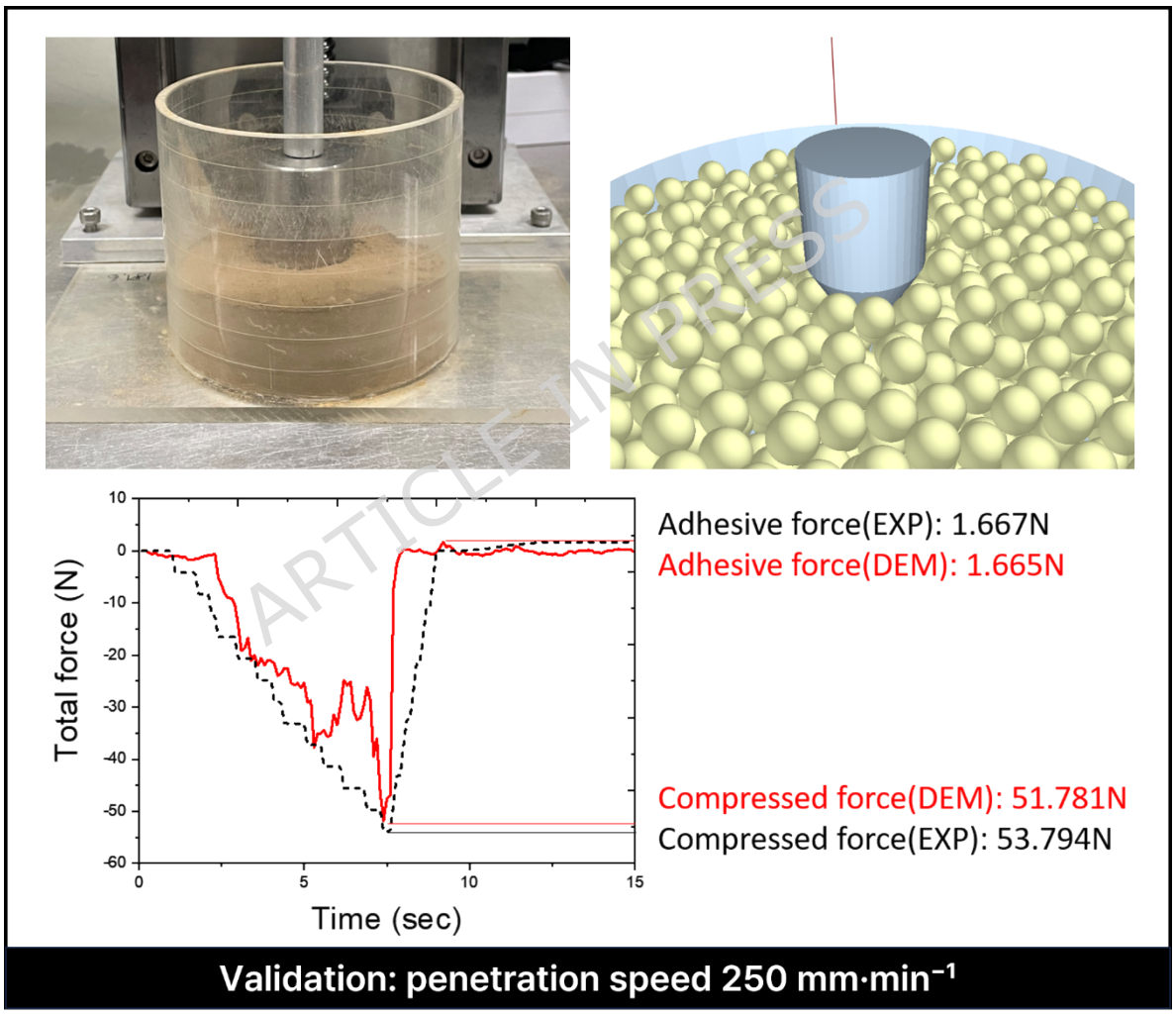

Fig. 11. Comparison between experimental and DEM-predicted compressive and adhesive force for sandy clay loam at 20% water content at 250 mm·min^{-1}.